Journal of Materials Chemistry A

ROYAL SOCIETY OF CHEMISTRY

PAPER

View Article Online
View Journal | View Issue

Check for updates

Cite this: J. Mater. Chem. A, 2024, 12, 27443

Controlled charge injection into nitrogen for efficient electrochemical nitrogen reduction based on metal-on-boron compound catalysts†

Yunji Han,‡[ab] Mihyeon Jo,‡[ab] Hyung-Kyu Lim *[c] and Sangheon Lee *[ab]

Received 19th June 2024
Accepted 12th August 2024

DOI: 10.1039/d4ta04256e

rsc.li/materials-a

This theoretical investigation explores sustainable methods for ammonia synthesis by evaluating the effectiveness of dual-atom catalysts composed of transition metals anchored on boron α- and β_{12}-sheet substrates for the electrochemical nitrogen reduction reaction. Utilizing density-functional theory, this study identifies enhancements in N_2 adsorption capabilities, crucial for mitigating kinetic limitations in the electrochemical nitrogen reduction reaction. The research delves into the charge redistribution mechanisms between the catalyst and nitrogen, emphasizing the pivotal role of metal oxidation states and charge injection into nitrogen in influencing nitrogen binding and subsequent electrochemical reduction steps. Furthermore, this work defines optimal conditions for catalytic efficiency by identifying a specific range for the binding strength of reaction intermediates, ensuring the effectiveness of the Sabatier principle in terms of N_2 binding. These insights significantly enhance the current understanding of catalyst design for the electrochemical nitrogen reduction reaction and provide a robust theoretical foundation for developing more efficient ammonia production systems.

Introduction

Ammonia (NH_3) is a multi-functional compound that is essential for manufacturing a variety of products including fertilizers, chemicals, and pharmaceuticals, as well as textiles.[1–3] Additionally, it is recognized as a valuable asset in modern chemical industries for its role as a hydrogen storage medium and carrier. This is primarily due to its high hydrogen content and environmentally benign combustion byproducts, namely nitrogen (N_2) and water (H_2O). In particular, the importance of ammonia for hydrogen storage and transportation is accentuated, as hydrogen gains attention as a sustainable alternative to carbon dioxide-intensive fossil fuels.[4–6] To realize economically affordable NH_3-based energy utilization, numerous efforts are being made to develop energy-efficient technologies to artificially synthesize NH_3 from N_2, which is abundant in the atmosphere of Earth.[7–10]

The traditional method for ammonia synthesis, the Haber-Bosch process ($N_2 + 3H_2 \rightarrow 2NH_3$), is energy-intensive, requiring high temperatures (400–500 °C) and pressures (150–300 bar) to break the strong triple bond of a dinitrogen molecule (bond dissociation energy = 225 kcal mol^{-1}).[11,12] Despite its high energy consumption, accounting for about 2% of the global energy supply, and associated greenhouse gas emissions, this process remains the dominant industrial method for ammonia production. Accordingly, there is a growing emphasis on developing alternative ammonia synthesis routes that are both energy-efficient and devoid of fossil fuel dependence.

The electrochemical nitrogen reduction reaction (eNRR) ($N_2 + 6H^+ + 6e^- \rightarrow 2NH_3$), which converts abundant atmospheric N_2 to NH_3, offers multiple advantages over the traditional Haber-Bosch process.[13–16] Specifically, the eNRR operates under less stringent conditions, such as room temperature and atmospheric pressure, and has the potential to be powered by renewable electrical energy sources like wind and solar. This capability significantly reduces the overall carbon footprint for ammonia production. Although the equilibrium potential under aqueous conditions is +0.092 V_{RHE},[17] complete conversion of N_2 to NH_3 under eNRR conditions requires a considerable overpotential due to the significant thermodynamic and kinetic barriers at each elementary step involved in the reductive addition of hydrogen to N_2.[18,19] While numerous experimental studies have been conducted to explore various types of materials – including pure metals,[20,21] metal alloys,[22–24] metal oxides,[25,26] metal nitrides, and metal phosphides[27,28] – the overpotential and faradaic efficiency have not yet reached levels suitable for commercial application. In this regard, it is necessary to overcome challenges like high overpotentials and low

[a]Department of Chemical Engineering and Materials Science, Ewha Womans University, 52, Ewhayeodae-gil, Seodaemun-gu, Seoul 03760, Republic of Korea. E-mail: sang@ewha.ac.kr

[b]Graduate Program in System Health Science and Engineering, Ewha Womans University, 52, Ewhayeodae-gil, Seodaemun-gu, Seoul 03760, Republic of Korea

[c]Division of Chemical Engineering and Bioengineering, Kangwon National University, Chuncheon, Gangwon-do 24341, Republic of Korea. E-mail: hklim@kangwon.ac.kr

† Electronic supplementary information (ESI) available. See DOI: https://doi.org/10.1039/d4ta04256e

‡ The two authors contributed equally.

faradaic efficiencies by fine-tuning catalyst structures at the atomic level, based on a thorough understanding of the reactivity at each elementary step.

In recent years, single-atom catalysts (SACs) have received significant attention for their high catalytic efficiency, selectivity, and stability in various catalytic reactions.[29–32] These catalysts are noteworthy because they allow for the more efficient use of precious metals and offer tunable active site configurations. Additionally, SACs provide a foundational framework for catalyst design, both experimentally and theoretically. Recently, the focus has also shifted toward dual-atom catalysts (DACs).[33–41] These catalysts feature two closely adjacent metal atoms embedded in suitable substrates, such as N-doped carbons, graphitic carbon nitride (g-C_3N_4), or boron nitrides. DACs are thought to offer a synergistic effect, potentially improving both catalytic activity and durability compared to SACs. Notably, there has been a growing trend in computational active-site screening studies based on density-functional theory (DFT), especially in the field of the eNRR for SACs and DACs.[36,42,43] Computational studies have demonstrated significant eNRR activity with various catalysts, including Fe–Rh anchored on nitrogen-doped graphene, showing an onset potential of −0.22 V_{CHE}. Other notable examples are single V atoms anchored on boron β_{12}-sheets with an onset potential of −0.28 V_{CHE} and single B atoms supported on holey g-C_3N_4, which exhibited an exceptionally low overpotential of −0.15 V_{CHE}.

Recently, boron sheets have emerged as candidate support materials for SACs or DACs, exhibiting 2D network structures with sp^2 hybridization similar to graphene.[44–47] These sheets are not only energetically stable but are also expected to have a range of chemical applications. Among the various boron sheet structures proposed, those with hexagonal holes inducing triangular lattice arrangements, such as α-sheets, and β_{12}-sheets, have been theoretically confirmed as the most stable. In particular, the work by Er *et al.* shows that boron sheets facilitate easier metal atom adsorption than graphene due to their electron-deficient nature.[48] Subsequently, the DFT study by Liu *et al.* suggests enhanced catalytic activity in the eNRR for Ru-doped boron α-sheet and β_{12}-sheet SACs with low limiting potentials of ΔG_{max} = 0.42 and 0.44 eV for Ru on α- and β_{12}-sheets, respectively.[49] Despite the promising catalytic activities in terms of limiting potential, these SACs suffer from the problem that the non-electrochemical N_2 adsorption step is thermodynamically unfavorable, so the overall eNRR rate is likely to be limited even if sufficiently high potentials are provided. These calculation results for Ru-doped boron sheet SACs indicate that for boron sheet catalysts to be competitive in the field of the eNRR, appropriate strategies must be jointly pursued to overcome the thermodynamically less favorable N_2 adsorption step while minimizing the magnitude of the limiting potential. While various theoretical studies on DAC-based electrocatalyst screening have been conducted,[33,50,51] research on the NRR using boron-sheet-based catalysts is still lacking. By addressing this unexplored area, our study aims to fill this gap in the literature and provides important insights into catalyst design for the NRR.

In this study, we perform additional DFT-based active-site screening for boron sheet eNRR catalysts by investigating the eNRR activity, when various transition metals (TMs) are doubly anchored onto boron α-sheets and β_{12}-sheets in the form of a DAC. As a result, we gain insight into the design principles of metal-doped boron sheet catalysts applicable for overcoming the key kinetic limitations associated with the eNRR. Subsequent in-depth electronic structure analysis provides theoretical evidence on how electronic interactions between the doped metal and boron sheet regulate the eNRR activity in a positive direction. The insights from this theoretical work are expected to serve as a robust foundation for designing experimental approaches aimed at refining eNRR catalyst systems.

Computational methods

In this work, spin-polarized DFT calculations are conducted using the Vienna *Ab initio* Simulation Package (VASP).[52] The projector-augmented plane wave (PAW) method is employed to model the interactions between core and valence electrons.[53] For the exchange-correlation term, the generalized gradient approximation (GGA) with the revised Perdew–Burke–Ernzerhof (RPBE) is used.[54] A cut-off energy of 400 eV was used for the plane wave expansion of electronic eigenfunctions. Convergence criteria for geometry optimization are established based on an energy difference less than 1×10^{-4} eV. Every surface model is constructed based on a supercell of hexagonal boron sheets with a vacuum space of 15 Å along the *z*-direction to avoid the interactions between periodic layers. For Brillouin zone integration, a $(3 \times 3 \times 1)$ Monkhorst–Pack *k*-point mesh is utilized for all catalyst models.

The adsorption energy ($\Delta E_{ads,M}$) of a species M (M = N_2 and its reaction intermediates) is calculated as the energy difference between the adsorption system (E_{*M}), the gas-phase adsorbate molecule (E_M), and the free-standing surface (E_*), using the following equation:

$$\Delta E_{ads,M} = E_{*M} - E_* - E_M \quad (1)$$

Note that the greater the $\Delta E_{ads,M}$ is along the negative direction, the stronger the adsorption strength of a species M is, and *vice versa*. The Gibbs free energy change (ΔG) for each elementary reaction step involving the proton coupled electron transfer (PCET) process is calculated using the computational hydrogen electrode (CHE) model.[55] In the CHE model, the Gibbs free energy of ($H^+ + e^-$) is defined as the free energy of $1/2H_2$ in the gas-phase. Thus, the ΔG change is computed using the following equation:

$$\Delta G = \Delta E_{elec} + \Delta E_{vib} - T\Delta S_{vib} + \Delta G_{solv} \quad (2)$$

where ΔE_{elec}, ΔE_{vib}, T, ΔS_{vib}, and ΔG_{solv} are the self-consistent electronic energy difference, the vibrational energy difference, the system temperature (298.15 K), the vibrational entropy change, and the solvation free energy change, respectively. The vibrational entropies and energies of the adsorption system are calculated from the vibrational frequencies with all atoms fixed except for the adsorbate and TMs. The solvation effect on the

reaction intermediates is calculated using the implicit solvation model, VASPsol,[56] where we use single point solvation free energy to consider the effect of water solvent. To reduce computational cost, vibrational and solvation data from Ru-doped models (Table S1†) are applied to other TMs.

We perform crystal orbital Hamilton population (COHP) analysis using the Local-Orbital Basis Suite Towards Electronic-Structure Reconstruction (LOBSTER) package.[57,58]

Results and discussion

Variability in dual-atom ensembles and N_2 adsorption

Catalyst models for DACs, based on boron α- and β_{12}-sheets, along with the TM species used for active site screening, are shown in Fig. 1a. Selected candidate species for active sites are TMs from the 4th and 5th periods, with d-orbital occupations ranging from d_2 to d_{10}. Models of the boron sheets are generated based on a previous theoretical study.[49] For α- and β_{12}-sheets, the ensemble effect is expected to vary due to different inter-vacancy distances: 5.09 Å and 2.98 Å for α-sheets and for β_{12}-sheets, respectively. After embedding the TMs, the optimized distances between active sites are altered based on their interactions with both the substrate and each other (Table S2†). In the case of α-sheets, these distances remain almost identical (5.13–5.14 Å) to the original inter-vacancy distance, indicating minimal interaction between the TMs. Conversely, for β_{12}-sheets, the active site distances generally shorten (2.29–3.06 Å) compared to the original inter-vacancy distance (2.98 Å), which implies significant metal–metal interactions. The improved formation energy of DACs (ΔE_f) on β_{12}-sheets (−0.30 to 1.40 eV) when compared to that on α-sheets (0.40–2.44 eV) also supports an additional metal–metal stabilization effect. Meanwhile, when the calculated formation energy is compared to that of Pd, Pt, and Ru on CeO_2 supports as synthesized experimentally (Table S3†), it is evident that the boron-sheet-based SAC and DAC catalysts can be formed with considerable stability. This reveals that β_{12}-sheets create distinct DAC ensemble structures with metal–metal interactions that are stably bound to vacancies without aggregation, while α-sheet DAC structures can be considered simple combinations of SACs.

The first step in the eNRR process is the adsorption of N_2, which is one of the fundamental factors for determining the performance of a catalyst. Due to the inert nature of N_2 molecules, they often fail to adsorb onto conventional catalyst surfaces, resulting in a kinetically unfavorable aspect for initiating the overall reaction.[59] To determine the most stable N_2 adsorption geometries on our DAC models, we optimize various possible N_2 adsorption configurations with different orientations and symmetries, as illustrated in Fig. 1b. For the α-sheets, the distance between the active TM sites is relatively large, resulting in two adsorption modes: "end-on" where the N_2 molecule adsorbs perpendicularly to a single active site, and "side-on" where the adsorbed N_2 molecule is aligned parallel to the surface between two active sites. For the β_{12}-sheet, the proximity of the active sites allows for two additional configurations, resulting in a total of four modes including "symmetric end-on" and "asymmetric side-on" modes in addition to "end-on" and "side-on" modes. It is important to note that the kinetic diameter of N_2 (3.64 Å) is larger than the inter-vacancy distance in β_{12}-sheets (2.98 Å). For chemisorption on catalyst surfaces, the actual bond length of N_2 (1.01 Å) is more relevant to the reaction than the kinetic diameter of N_2. The N_2 bond length is

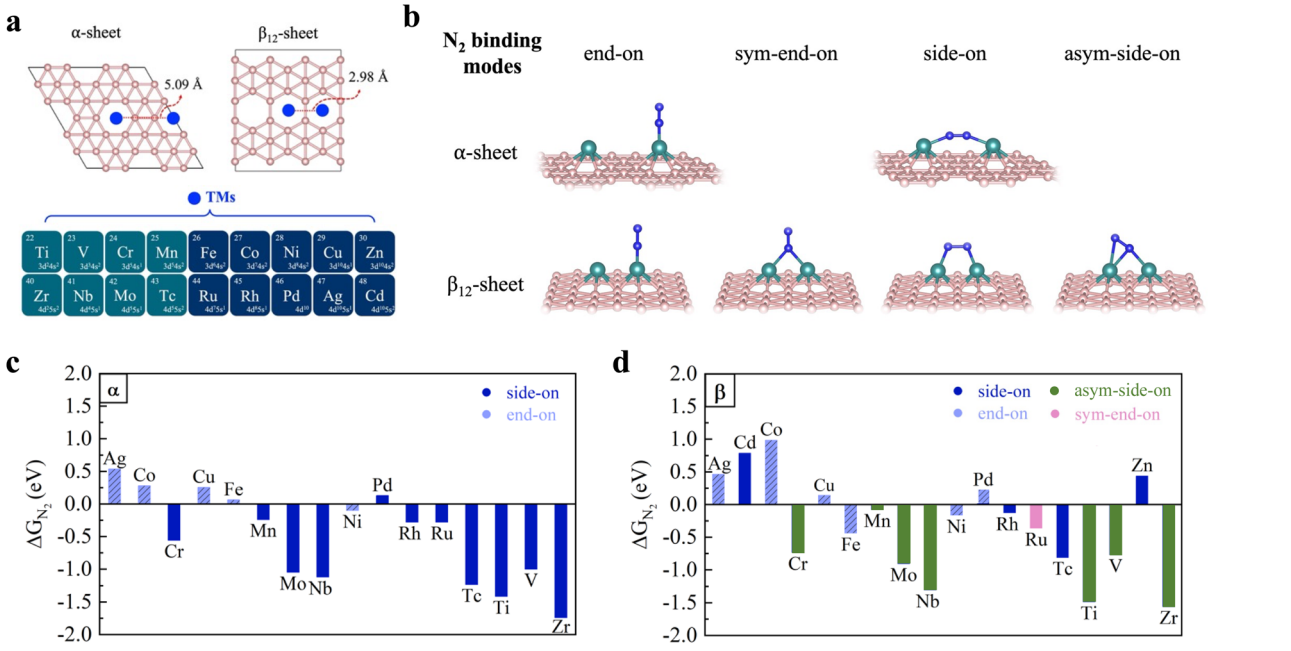

Fig. 1 (a) Dual-atom catalyst models based on boron α- and β_{12}-sheets, and a range of transition metals used for catalyst screening. (b) Various possible N_2 binding configurations on DACs based on α- and β_{12}-sheets. The most stable N_2 adsorption structures and energies for (c) α-sheets and (d) β_{12}-sheets.

significantly smaller than the inter-vacancy distance in the β_{12}-sheet. Our DFT calculations show that upon metal atom adsorption, the distance between metal atoms in β_{12}-sheets is long enough to accommodate N_2 molecules in various configurations. Our detailed analyses of the possible N_2 binding configurations, considering the actual molecular dimensions and the structural characteristics of our catalyst system, confirm the feasibility of all binding modes presented in Fig. 1b.

Fig. 1c and d show the most stable N_2 adsorption energies and structures for each dual-atom TM embedded in boron α- and β_{12}-sheets, respectively. For the α-sheet, most TMs, except Ag, Co, Cu, Fe, and Pd, form stable adsorption structures in the side-on configuration with negative adsorption free energies. In particular, Cr, Mo, Nb, Tc, Ti, V, and Zr exhibit significantly strong N_2 fixation effects with adsorption free energies ranging from -0.55 eV up to -1.75 eV. These calculation results indicate that despite the relatively long distance between the TM sites, the incorporation of dual-atom TMs within a boron α-sheet enables stable N_2 chemisorption on the TMs in the side-on configuration. This can be attributed to the structural flexibility of the boron sheet, resulting in optimized N_2 adsorption structures with reduced metal–metal distances, initially from 5.13 Å to 4.40–4.75 Å (Table S4 and Fig. S1†). For the β_{12}-sheet, more complicated N_2 adsorption characteristics, due to the ensemble effects between the two closely spaced active sites, result in a variety of N_2 adsorption structures with often marginal energy differences between different configurations. Nevertheless, similar to the α-sheet, the majority of stable N_2 adsorption structures on the β_{12}-sheet are of the side-on configurations, and strong adsorption cases are found exclusively in the asymmetric side-on configuration. Note that the metal–metal distances of the β_{12}-sheet are marginally affected by N_2 adsorption compared to those of the α-sheet (Table S4†). This indicates that the arrangement of metal active sites in the β_{12}-sheet is structurally highly conducive to N_2 adsorption.

Charge transfer effect for strong N_2 adsorption

From Bader charge analysis,[60] we find that there are significant charge transfer tendencies between TMs and boron sheets. For the bare surfaces of boron-based DACs, the average partial charges at the TMs range from -0.10 to $1.19|e|$ for α-sheets and -0.04 to $1.04|e|$ for β_{12}-sheets, as summarized in Table S5.† These analysis results indicate that for most cases of our boron-based DACs, charge transfer occurs from the active TMs to the boron substrate, resulting in positively charged TM active sites. We find in Fig. 2a and b that there are notable correlations between the N_2 adsorption strength and the partial charge of the active site for both α- and β_{12}-sheet cases. These observed

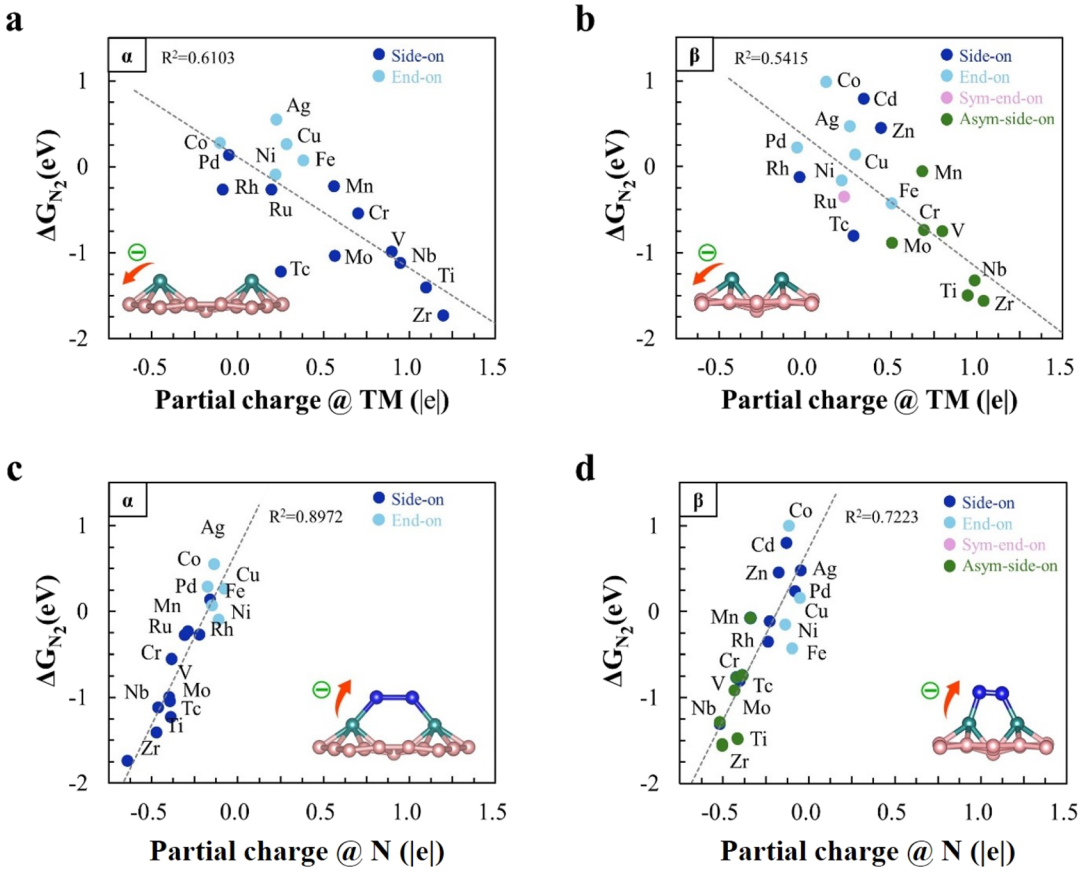

Fig. 2 Average partial charge of TMs in bare DACs for (a) α-sheets (denoted as α) and (b) β_{12}-sheets (denoted as β). Average partial charge of a N_2 molecule adsorbed on DACs for (c) α-sheets (denoted as α) and (d) β_{12}-sheets (denoted as β).

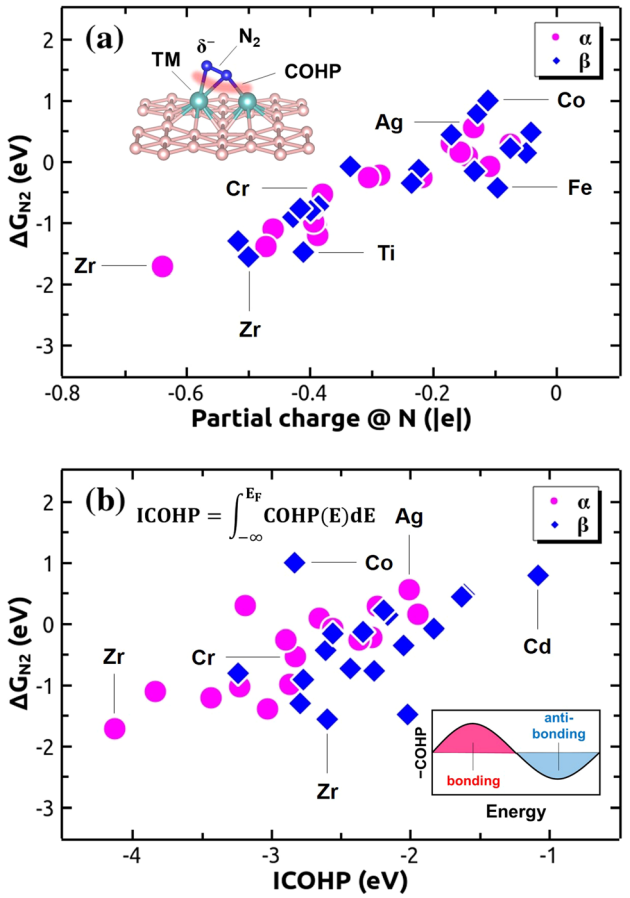

Fig. 3 (a) Calculated N_2 adsorption free energies as a function of (a) the average partial charge of a N_2 molecule adsorbed on DACs and (b) COHP-calculated metal–N_2 binding strength on α-sheets (denoted as α) and β_{12}-sheets (denoted as β) for the most stable N_2 adsorption structures (see Fig. 1). Refer to raw data in Table S7.†

correlations suggest that the more positively charged (or higher in oxidation state) the active site is, the stronger the interaction with N_2 tends to be. This analysis result is consistent with previous theoretical studies on SACs.[61,62]

To further elucidate the electronic structural origins of this trend, we conduct additional analyses including partial density of states (pDOS) and crystal orbital Hamilton population (COHP) analyses (Fig. S2–S5†). The pDOS analysis reveals that there is a correlation between the N_2 adsorption strength and the formation of bonding orbitals between metal d orbitals and N 2p orbitals near the Fermi level. As shown in Fig. 3a, we find that the metal–N_2 binding strength tends to increase as the amount of charge transfer to N_2 increases. Moreover, COHP analysis demonstrates that there is a strong correlation between the COHP-calculated metal–N_2 binding strength and the N_2 binding free energy, as shown in Fig. 3b. These results provide a more comprehensive understanding of the N_2 activation mechanism, showing that the NRR thermodynamics of the TM active sites exhibit systematic variations from both classical charge transfer and orbital interaction perspectives. This interpretation of bonding characteristics from dual perspectives offers valuable insights into the rational design of more efficient NRR catalysts, highlighting the importance of electronic structure engineering for optimizing catalyst performance.

These types of positively charged active sites are also known to be beneficial in suppressing competitive hydrogen evolution reactions due to the enhanced electrostatic repulsion with protons. One may wonder whether the positively charged active sites could be poisoned by H_2O or OH adsorption. Our calculations of water molecule adsorption on these oxidized active sites revealed that, with the exception of group 4 and 5 metals such as Nb, Ti, V, and Zr (which have the highest oxidation states), water adsorption is either difficult or weak (Fig. S6 and Table S9†). This suggests that for most of the active sites, side reactions related to water molecules are unlikely to have a significant impact on the NRR process.

Further analysis using N_2 adsorbed models shows that the adsorbed N_2 tends to be negatively charged, with adsorption strength being proportional to the negative partial charge on N_2 (Fig. 2c, d and Table S6†). This indicates that electrons are transferred to the N_2 molecule, with the transfer reaching levels up to approximately one electron per molecule. This implies that boron-based DACs can overcome the challenges of electron injection, which are typically hindered by the strongly negative electron affinity (−1.9 eV) of the N_2 molecule.[63] It is worth noting that electrons taken up by N_2 mostly transferred from the TM active site (Table S8 and Fig. S7†). This suggests that TM active sites on the boron surface have the capability to transfer additional electrons to the adsorbate. Therefore, a fundamental correlation is confirmed that the strength of N_2 binding correlates with the oxidation tendencies of the TM species, which is supported by the positive correlation between the ionization energy of TMs and N_2 binding energy (Fig. S8†). Considering the maximum N_2 adsorption free energy of around −0.5 eV in a previous boron-based SAC study,[49] the dual-atom ensemble formation of DACs enables tight side-on interactions with N_2, thereby achieving more stable bonding with enhanced electron transfer.

The first PCET step for N_2H formation

The first PCET leading to the formation of the N_2H binding state is considered another critical factor in the eNRR, especially due to the low proton affinity and negative electron affinity of the N_2 molecule.[18] In the boron-based DACs examined in this study, electron injection into N_2 occurs upon adsorption, potentially facilitating the formation of N_2H through the first PCET step. This expectation is supported by the strong linear correlation between the binding free energies of N_2 and N_2H, as shown in Fig. 4a and b. This suggests that strong adsorption, driven by electron transfer to N_2, significantly eases the first PCET step. The binding energy of further reaction intermediates (N_2H_2, N_2H_3, *etc.*), which will be discussed later in the eNRR pathway, also shows strong linear correlations with that of N_2 (Fig. S9 and S10†). This indicates that the TM active sites in boron-based DACs adhere to the linear scaling relationship typically observed in TM-based catalysts,[64,65] suggesting a volcano-type trade-off in the overall catalytic activity.

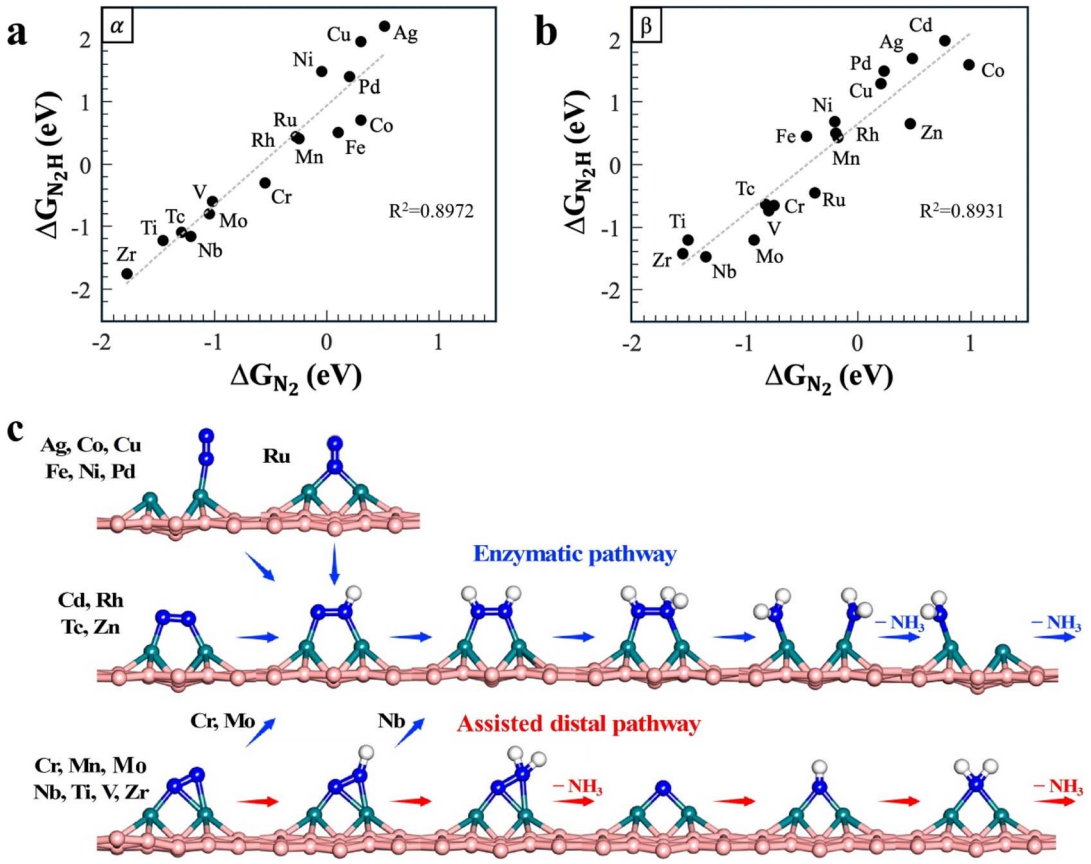

Fig. 4 Correlation between N_2 and N_2H binding free energies for (a) α-sheets (denoted as α) and (b) β_{12}-sheets (denoted as β). (c) Selected eNRR pathways depending on the N_2 binding structures.

The conventional eNRR pathways can be categorized into distal and enzymatic pathways, depending on the starting N_2 binding structure (Fig. S11†).[59] In the distal pathway, the first three PCETs for the formation of the first NH_3 molecule occur on the distal nitrogen atom in end-on modes. Subsequently, the following three PCETs take place on the remaining single nitrogen atom to form another NH_3 molecule. In the enzymatic pathway, due to the symmetric nature of the N_2 binding in a side-on configuration, six consecutive PCETs take place alternately on both nitrogen atoms, resulting in the formation of two NH_3 molecules in the final two steps. In the α-sheets, the large distance between active sites clearly differentiates between end-on and side-on N_2 binding modes, leading to distinct distal (Ag, Co, Cu, Fe, and Ni) and enzymatic reaction pathways (rest of the TMs). In contrast, the β_{12}-sheets feature shorter distances between active sites, resulting in minor variations in N_2 binding energy depending on the structure. Consequently, the binding mode of reaction intermediates may change during consecutive PCET steps due to the ensemble effect of dual active sites. This suggests that the most feasible reaction pathway is not solely dependent on the initial N_2 binding mode. Investigations into the possible binding modes of N_2H and N_2H_2 identify the most stable configurations for each TM, leading to the conclusion that the eNRR pathway for the β_{12}-sheet follows the conventional enzymatic and assisted distal pathways (Fig. 4c). As a result, every TM with end-on (Ag, Co, Cu, Fe, Ni, and Pd) and symmetric end-on (Ru) N_2 binding stabilizes into a symmetric side-on N_2H binding mode, thus adhering to the enzymatic pathway. Additionally, among the asymmetric side-on TMs, Cr, Mo, and Nb shift to the enzymatic pathway after the 1st and 2nd PCET steps, respectively, while the remaining TMs follow the assisted distal pathway.

Characteristics of overall eNRR thermodynamics

The free energy profiles of eNRR pathways for each TM are calculated to assess overall reaction thermodynamics and theoretical limiting potentials (E^0_{theo}). Theoretical limiting potentials are derived from the highest energy barriers (ΔG_{max}) in the PCET steps, using the Nernst equation ($\Delta G_{max} = -FE^0_{theo}$). These E^0_{theo} values are plotted against N_2H binding free energy in Fig. 5a and b for α- and β_{12}-sheets, respectively. The choice of N_2H as a reference is due to its greater influence on determining the reaction pathway compared to N_2 adsorption. Both profiles exhibit clear volcano-type behavior, with optimal limiting potentials around an N_2H binding free energy of approximately +0.2 eV, indicating weak chemisorption of N_2. This pattern underscores the effectiveness of the Sabatier principle in boron-based DAC systems. The top three TM active sites are Fe, Mn, and Rh for α-sheets (E^0_{theo} values of −0.47, −0.51, and −0.61 V_{CHE}, respectively), and Fe, Rh, and Ru for β_{12}-

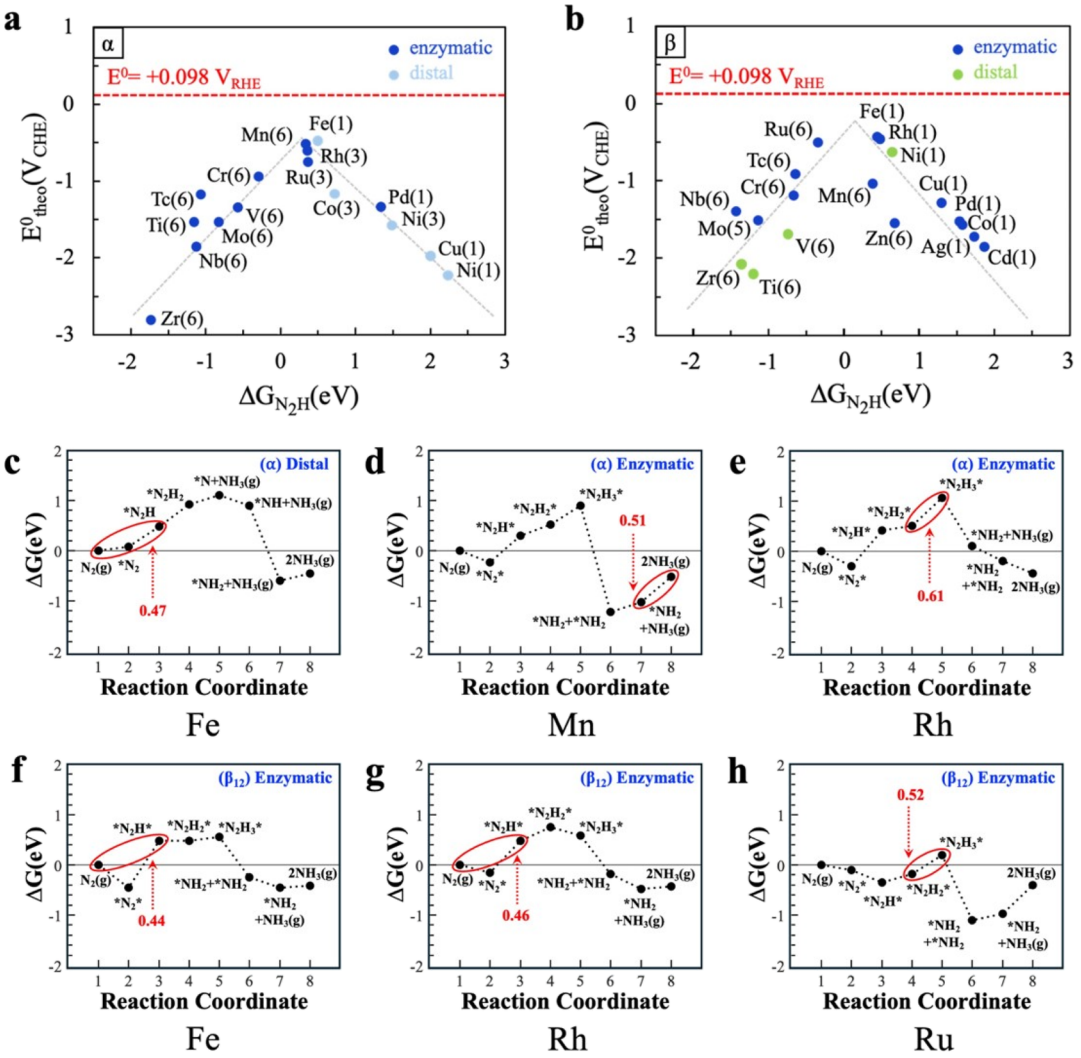

Fig. 5 Volcano plot of eNRR limiting potentials for (a) α-sheets (denoted as α) and (b) β_{12}-sheets (denoted as β). Reaction free energy profiles for (c) Fe, (d) Mn, and (e) Rh on α-sheets, and for (f) Fe, (g) Rh, and (h) Ru on β_{12}-sheets. The potential-determining step (PDS) for each catalyst is indicated by the number in the parenthesis in graphs (a) and (b).

sheets (E^0_{theo} values of −0.44, −0.46, and −0.52 V_{CHE}, respectively). Although individual TM active sites exhibit variations in reaction thermodynamics depending on the boron sheet and configuration of reaction intermediates, the overall eNRR performance for α- and β_{12}-sheets remains in a similar range. Detailed reaction energy profiles for the top three catalysts in each boron sheet are presented in Fig. 5c–h, while those for the remaining TMs are shown in Fig. S12 and S13.† We find that the limiting potential-determining step (PDS) typically occurs during the initial PCET steps when N_2 binding is unfavorable and in the latter PCET steps when N_2 binding is favorable.

Achieving optimal N_2 binding on the catalyst surfaces significantly impacts the kinetics of the eNRR, particularly by lowering the energy barrier associated with the first PCET step. This adjustment is crucial because the initial PCET step has traditionally been a significant kinetic bottleneck in the eNRR process due to the inherently low proton affinity and negative electron affinity of the N_2 molecule. By fine-tuning active sites of the catalyst to enhance N_2 adsorption, the electron density around the N_2 molecule can be effectively increased, facilitating easier proton attachment and reducing the energy required for this critical step. Consequently, this optimized N_2 binding not only decreases the activation energy barrier but also enhances the overall reaction kinetics, making the eNRR process more efficient and potentially more competitive with traditional ammonia synthesis methods. Furthermore, to achieve ideal catalyst performance with equally distributed reaction energies across all PCET steps, future research should also focus on breaking the linear scaling relationships observed in current catalyst systems. This insight underscores the importance of designing catalysts with precise control over N_2 adsorption characteristics to overcome the kinetic challenges and improve the efficiency of ammonia production *via* electrochemical methods.

Conclusions

This theoretical investigation provides a comprehensive framework for understanding the eNRR using TM-based DACs anchored on boron α- and β_{12}-sheets. The study highlights that the enhancement in N_2 adsorption, a crucial factor for overcoming kinetic barriers in the eNRR, is facilitated by dual-atom active sites, positioning this catalyst system as a potential new platform for N_2 fixation. A detailed analysis of charge transfer mechanisms underscores the critical role of the oxidation state of transition metals in N_2 binding. Our calculation results demonstrate the important role of the metal oxidation state and charge injection into nitrogen in influencing the thermodynamics of nitrogen binding and subsequent electrochemical reduction steps. These insights add depth to the existing theoretical knowledge on eNRR catalysts and provide a valuable foundation for future experimental strategies. This study also identifies optimal thermodynamic conditions for the eNRR, specifying the range of binding free energies of key reaction intermediates that ensures the best catalytic performance. Finally, these theoretical findings are expected to greatly contribute to the development of enhanced electrochemical systems for sustainable ammonia production.

Data availability

The data supporting this article have been included as part of the ESI.†

Author contributions

Yunji Han: investigation, formal analysis, writing – original draft. Mihyeon Jo: investigation, formal analysis, writing – original draft. Hyung-Kyu Lim: conceptualization, supervision, writing – original draft & review. Sangheon Lee: conceptualization, supervision, writing – original draft & review, project administration, funding acquisition.

Conflicts of interest

There are no conflicts to declare.

Acknowledgements

This work was supported by the National Research Foundation of Korea grant funded by the Ministry of Science and ICT (NRF-2022M3J1A1085384 and NRF-2023R1A2C1006648). This work was also supported by the Korea Planning & Evaluation of Industrial Technology grant funded by the Ministry of Trade, Industry and Energy (RS-2023-00267003).

References

1 J. N. Galloway, A. R. Townsend, J. W. Erisman, M. Bekunda, Z. Cai, J. R. Freney, L. A. Martinelli, S. P. Seitzinger and M. A. Sutton, *Science*, 2008, **320**, 889–892.
2 K. Honkala, A. Hellman, I. N. Remediakis, A. Logadottir, A. Carlsson, S. Dahl, C. H. Christensen and J. K. Nørskov, *Science*, 2005, **307**, 555–558.
3 J. H. Montoya, C. Tsai, A. Vojvodic and J. K. Nørskov, *ChemSusChem*, 2015, **8**, 2180–2186.
4 D. V. Yandulov and R. R. Schrock, *Science*, 2003, **301**, 76–78.
5 A. Klerke, C. H. Christensen, J. K. Nørskov and T. Vegge, *J. Mater. Chem.*, 2008, **18**, 2304–2310.
6 S. Giddey, S. P. S. Badwal and A. Kulkarni, *Int. J. Hydrogen Energy*, 2013, **38**, 14576–14594.
7 W. Qiu, X.-Y. Xie, J. Qiu, W.-H. Fang, R. Liang, X. Ren, X. Ji, G. Cui, A. M. Asiri, G. Cui, B. Tang and X. Sun, *Nat. Commun.*, 2018, **9**, 3485.
8 B. A. MacKay and M. D. Fryzuk, *Chem. Rev.*, 2004, **104**, 385–402.
9 T. Shima, S. Hu, G. Luo, X. Kang, Y. Luo and Z. Hou, *Science*, 2013, **340**, 1549–1552.
10 K. C. MacLeod and P. L. Holland, *Nat. Chem.*, 2013, **5**, 559–565.
11 H. Liu, *Chin. J. Catal.*, 2014, **35**, 1619–1640.
12 J. Humphreys, R. Lan and S. Tao, *Adv. Energy Sustainability Res.*, 2021, **2**, 2000043.
13 D. Bao, Q. Zhang, F.-L. Meng, H.-X. Zhong, M.-M. Shi, Y. Zhang, J.-M. Yan, Q. Jiang and X.-B. Zhang, *Adv. Mater.*, 2017, **29**, 1604799.
14 W. Guo, K. Zhang, Z. Liang, R. Zou and Q. Xu, *Chem. Soc. Rev.*, 2019, **48**, 5658–5716.
15 X. Cui, C. Tang and Q. Zhang, *Adv. Energy Mater.*, 2018, **8**, 1800369.
16 G.-F. Chen, S. Ren, L. Zhang, H. Cheng, Y. Luo, K. Zhu, L.-X. Ding and H. Wang, *Small Methods*, 2019, **3**, 1800337.
17 H. Shen, C. Choi, J. Masa, X. Li, J. Qiu, Y. Jung and Z. Sun, *Chem*, 2021, **7**, 1708–1754.
18 A. Kaiprathu, P. Velayudham, H. Teller and A. Schechter, *J. Solid State Electrochem.*, 2022, **26**, 1897–1917.
19 N. Cherkasov, A. O. Ibhadon and P. Fitzpatrick, *Chem. Eng. Process.*, 2015, **90**, 24–33.
20 A. Logadottir, T. H. Rod, J. K. Nørskov, B. Hammer, S. Dahl and C. J. H. Jacobsen, *J. Catal.*, 2001, **197**, 229–231.
21 H.-M. Liu, S.-H. Han, Y. Zhao, Y.-Y. Zhu, X.-L. Tian, J.-H. Zeng, J.-X. Jiang, B. Y. Xia and Y. Chen, *J. Mater. Chem. A*, 2018, **6**, 3211–3217.
22 F. Pang, Z. Wang, K. Zhang, J. He, W. Zhang, C. Guo and Y. Ding, *Nano Energy*, 2019, **58**, 834–841.
23 D. Chen, Q. Yao, P. Cui, H. Liu, J. Xie and J. Yang, *ACS Appl. Energy Mater.*, 2018, **1**, 883–890.
24 W. Zhang, J. Yang and X. Lu, *ACS Nano*, 2012, **6**, 7397–7405.
25 Á. B. Höskuldsson, Y. Abghoui, A. B. Gunnarsdóttir and E. Skúlason, *ACS Sustain. Chem. Eng.*, 2017, **5**, 10327–10333.
26 B. Li, Y. Zhu and W. Guo, *Inorg. Chem. Front.*, 2023, **10**, 5812–5838.
27 Y. Ying, K. Fan, X. Luo and H. Huang, *J. Mater. Chem. A*, 2019, **7**, 11444–11451.
28 E. J. Popczun, J. R. McKone, C. G. Read, A. J. Biacchi, A. M. Wiltrout, N. S. Lewis and R. E. Schaak, *J. Am. Chem. Soc.*, 2013, **135**, 9267–9270.

29 X. Li, X. Yang, Y. Huang, T. Zhang and B. Liu, *Adv. Mater.*, 2019, **31**, 1902031.
30 X.-F. Yang, A. Wang, B. Qiao, J. Li, J. Liu and T. Zhang, *Acc. Chem. Res.*, 2013, **46**, 1740–1748.
31 Q. Qin, T. Heil, M. Antonietti and M. Oschatz, *Small Methods*, 2018, **2**, 1800202.
32 Y. Liu, Q. Xu, X. Fan, X. Quan, Y. Su, S. Chen, H. Yu and Z. Cai, *J. Mater. Chem. A*, 2019, **7**, 26358–26363.
33 L. Li, K. Yuan and Y. Chen, *Acc. Mater. Res.*, 2022, **3**, 584–596.
34 Z. W. Chen, J.-M. Yan and Q. Jiang, *Small Methods*, 2019, **3**, 1800291.
35 S.-h. Kim, H. C. Song, S. J. Yoo, J. Han, K.-Y. Lee and H. C. Ham, *J. Mater. Chem. A*, 2022, **10**, 6216–6230.
36 H. Li, Z. Zhao, Q. Cai, L. Yin and J. Zhao, *J. Mater. Chem. A*, 2020, **8**, 4533–4543.
37 X. Zhang, A. Chen, Z. Zhang and Z. Zhou, *J. Mater. Chem. A*, 2018, **6**, 18599–18604.
38 C. Wan, X. Liu, J. Wang, F. Chen and D.-G. Cheng, *Nano Res.*, 2023, **16**, 6260–6269.
39 C. Wan, G. Li, J. Wang, L. Xu, D.-g. Cheng, F. Chen, Y. Asakura, Y. Kang and Y. Yamauchi, *Angew. Chem., Int. Ed.*, 2023, **62**, e202305371.
40 C. Wan, R. Li, J. Wang, D.-g. Cheng, F. Chen, L. Xu, M. Gao, Y. Kang, M. Eguchi and Y. Yamauchi, *Angew. Chem., Int. Ed.*, 2024, **63**, e202404505.
41 Y. Kang, O. Cretu, J. Kikkawa, K. Kimoto, H. Nara, A. S. Nugraha, H. Kawamoto, M. Eguchi, T. Liao, Z. Sun, T. Asahi and Y. Yamauchi, *Nat. Commun.*, 2023, **14**, 4182.
42 H.-R. Zhu, Y.-L. Hu, S.-H. Wei and D.-Y. Hua, *J. Phys. Chem. C*, 2019, **123**, 4274–4281.
43 X. Lv, W. Wei, F. Li, B. Huang and Y. Dai, *Nano Lett.*, 2019, **19**, 6391–6399.
44 H. Tang and S. Ismail-Beigi, *Phys. Rev. Lett.*, 2007, **99**, 115501.
45 H. Liu, J. Gao and J. Zhao, *Sci. Rep.*, 2013, **3**, 3238.
46 X. Wu, J. Dai, Y. Zhao, Z. Zhuo, J. Yang and X. C. Zeng, *ACS Nano*, 2012, **6**, 7443–7453.
47 F. Ma, Y. Jiao, G. Gao, Y. Gu, A. Bilic, Z. Chen and A. Du, *Nano Lett.*, 2016, **16**, 3022–3028.
48 S. Er, G. A. de Wijs and G. Brocks, *J. Phys. Chem. C*, 2009, **113**, 18962–18967.
49 C. Liu, Q. Li, J. Zhang, Y. Jin, D. R. MacFarlane and C. Sun, *J. Mater. Chem. A*, 2019, **7**, 4771–4776.
50 Y. Li, Y. Li, H. Sun, L. Gao, X. Jin, Y. Li, Z. Lv, L. Xu, W. Liu and X. Sun, *Nano-Micro Lett.*, 2024, **16**, 139.
51 B. Pratihar, A. Jana, A. Kumar De and S. De, *ChemCatChem*, 2024, **16**, e202301527.
52 G. Kresse and J. Furthmüller, *Phys. Rev. B: Condens. Matter Mater. Phys.*, 1996, **54**, 11169–11186.
53 P. E. Blöchl, *Phys. Rev. B: Condens. Matter Mater. Phys.*, 1994, **50**, 17953–17979.
54 B. Hammer, L. B. Hansen and J. K. Nørskov, *Phys. Rev. B: Condens. Matter Mater. Phys.*, 1999, **59**, 7413–7421.
55 J. K. Nørskov, J. Rossmeisl, A. Logadottir, L. Lindqvist, J. R. Kitchin, T. Bligaard and H. Jónsson, *J. Phys. Chem. B*, 2004, **108**, 17886–17892.
56 K. Mathew, R. Sundararaman, K. Letchworth-Weaver, T. A. Arias and R. G. Hennig, *J. Chem. Phys.*, 2014, **140**, 084106.
57 R. Nelson, C. Ertural, J. George, V. L. Deringer, G. Hautier and R. Dronskowski, *J. Comput. Chem.*, 2020, **41**, 1931–1940.
58 R. Dronskowski and P. E. Bloechl, *J. Phys. Chem.*, 1993, **97**, 8617–8624.
59 C. J. M. van der Ham, M. T. M. Koper and D. G. H. Hetterscheid, *Chem. Soc. Rev.*, 2014, **43**, 5183–5191.
60 W. Tang, E. Sanville and G. Henkelman, *J. Phys.: Condens. Matter*, 2009, **21**, 084204.
61 N. Cheng, L. Zhang, K. Doyle-Davis and X. Sun, *Electrochem. Energy Rev.*, 2019, **2**, 539–573.
62 S. Back, J. Lim, N.-Y. Kim, Y.-H. Kim and Y. Jung, *Chem. Sci.*, 2017, **8**, 1090–1096.
63 A. Rovaletti, L. De Gioia, C. Greco and F. Arrigoni, *Dalton Trans.*, 2023, **52**, 7966–7974.
64 A. S. Raman and A. Vojvodic, *Handbook of Materials Modeling: Applications: Current and Emerging Materials*, ed. W. Andreoni and S. Yip, Springer International Publishing, Cham, 2020, pp. 1321–1341, DOI: **10.1007/978-3-319-44680-6_2**.
65 E. M. Fernández, P. G. Moses, A. Toftelund, H. A. Hansen, J. I. Martínez, F. Abild-Pedersen, J. Kleis, B. Hinnemann, J. Rossmeisl, T. Bligaard and J. K. Nørskov, *Angew. Chem., Int. Ed.*, 2008, **47**, 4683–4686.